Comparison of Two- and Three-field Formulation Discretizations for Flow and Solid Deformation in Heterogeneous Porous Media

Kadeethum, Teeratorn; Nick, Hamid; Lee, S.

Published in:
Proceedings of 20th Annual Conference of the International Association for Mathematical Geosciences

Publication date:
2019

Document Version
Peer reviewed version

Comparison of Two- and Three-field Formulation Discretizations for Flow and Solid Deformation in Heterogeneous Porous Media

T. Kadeethum[1*], H. M. Nick[1], and S. Lee[2]

[1]Technical University of Denmark, Denmark teekad@dtu.dk
[2]Florida State University, Florida, USA
[*] presenting author

Abstract

We illustrate the advantages and disadvantages among two- and three-field formulations that are used to mimic the flow and solid deformation in heterogeneous porous media. Local mass conservation, flux approximation, average permeability alteration at each time step, and degrees of freedom (DOF) are utilized to evaluate each method. Our result presents that four out of six methods provide the local mass conservative while three out of those four methods produce approximately the same flux approximation and permeability alteration. Three-field formulation methods generally require a smaller time step to converge for solving the system of nonlinear equations. Besides, they have more DOF than that of the two-field formulation because they have one more primary variable, i.e. fluid velocity. The two-field formulation that is a combination of continuous and enriched Galerkin function space enjoys all the benefits while requires the least DOF among the methods that preserve local mass conservation property.

1 Statement of problem

Let $\Omega \subset \mathbb{R}^d$ be the domain of interest in d-dimensional space bounded by boundary, $\partial\Omega$. $\partial\Omega$ can be decomposed to displacement and traction boundaries, $\partial\Omega_u$ and $\partial\Omega_t$, respectively, for the solid deformation problem. For the fluid flow problem, $\partial\Omega$ is decomposed to pressure and flux boundaries, $\partial\Omega_p$ and $\partial\Omega_q$, respectively. The time domain is denoted by $\mathbb{T} = (0, T]$ with $T > 0$. The coupling between the fluid flow and solid deformation can be captured through the application of Biot's equation of poroelasticity, which is composed of force and mass balance equations (Biot, 1941). The linear momentum balance equation is read as follows:

$$\nabla \cdot 2\mu_l \boldsymbol{\varepsilon} - \nabla \lambda_l \nabla \cdot \boldsymbol{u}\boldsymbol{I} + \alpha \nabla p = \boldsymbol{f} \text{ in } \Omega \times \mathbb{T}, \tag{1}$$

$$\boldsymbol{u} = \boldsymbol{u}_D \text{ on } \partial\Omega_u \times \mathbb{T} \text{ and } \boldsymbol{\sigma} \cdot \boldsymbol{n} = \sigma_D \text{ on } \partial\Omega_t \times \mathbb{T}, \tag{2}$$

where λ_l and μ_l are are Lamé constants, $\boldsymbol{\varepsilon}$ is strain, $\boldsymbol{u}$ is displacement vector, $\boldsymbol{I}$ is the second-order identity tensor, α is Biot's coefficient defined as $\alpha = 1 - \frac{K}{K_S}$, K is the bulk modulus of a rock matrix, K_s is bulk rock matrix material (e.g. solid grains), p is fluid pressure, $\boldsymbol{n}$ is a normal unit vector, $\boldsymbol{f}$ is body force vector, which is neglected in this study, $\boldsymbol{\sigma}$ is stress, $\boldsymbol{u_D}$ and σ_D are prescribed displacement and traction at boundaries, respectively.

The second equation is the mass balance equation, which is read as:

$$\rho\left(\phi c_f + \frac{\alpha - \phi}{K_s}\right)\frac{\partial p}{\partial t} + \rho\alpha\frac{\partial \nabla \cdot \boldsymbol{u}}{\partial t} - \nabla \cdot (\rho \boldsymbol{v}) = g \text{ in } \Omega \times \mathbb{T}, \tag{3}$$

$$\boldsymbol{v} = \nabla \cdot \frac{\boldsymbol{\kappa}}{\rho}(\nabla p - \rho \mathbf{g}) \text{ in } \Omega \times \mathbb{T}, \tag{4}$$

$$p = p_D \text{ on } \partial\Omega_p \times \mathbb{T} \text{ and } -\nabla \cdot \boldsymbol{\kappa}(\nabla p - \rho \mathbf{g}) \cdot \boldsymbol{n} = q_D \text{ on } \partial\Omega_q \times \mathbb{T}, \tag{5}$$

where ρ is fluid density, ϕ is initial porosity, c_f is fluid compressibility, t is time at the specific point, $\boldsymbol{v}$ is Darcy velocity vector, $\mathbf{g}$ is a gravitational vector, g is sink/source, p_D and q_D are

specified pressure and flux, respectively, and $\boldsymbol{\kappa}$ is hydraulic conductivity defined as $\boldsymbol{\kappa} = \frac{\rho \mathbf{k_m}}{\mu}$, $\boldsymbol{k_m}$ is matrix permeability tensor and μ is fluid viscosity. The rock displacement caused by changing in pore pressure can influence media conductivity by:

$$\boldsymbol{k_m} = \boldsymbol{k_{m0}} \left(1 + \varepsilon_v/\phi\right)^3 / \left(1 + \varepsilon_v\right), \tag{6}$$

where $\boldsymbol{k_{m0}}$ and $\boldsymbol{k_m}$ represent initial and current rock matrix permeability, respectively, and ε_v is a volumetric strain (Du and Wong, 2007).

There are six discretizations compared in this study. Three of discretizations are two-field formulation ($\boldsymbol{u}\times p$), and the rest are three-field formulation ($\boldsymbol{u}\times\boldsymbol{v}\times p$) as presented in Table 1. The details of two-field formulation discretization can be found in Lee et al. (2016), Choo and Lee (2018), and Kadeethum et al. (2019), while Haga et al. (2012) presents the details of three-field formulation discretization. The solving algorithm, solver settings, and coupling scheme can be found in Kadeethum et al. (2019). The Picard iteration is used to solve the nonlinear pressure-dependent k_m model, and the PETSc LU solver is used inside each iteration for solving the system of linear equations (Balay et al., 2018).

Formulation	Mixed space	Displacement	Velocity	Pressure
$\boldsymbol{u}\times p$	$\mathrm{CG}_2 \times \mathrm{CG}_1$	CG_2	-	CG_1
	$\mathrm{CG}_2 \times \mathrm{EG}_1$	CG_2	-	EG_1
	$\mathrm{CG}_2 \times \mathrm{DG}_1$	CG_2	-	DG_1
$\boldsymbol{u}\times\boldsymbol{v}\times p$	$\mathrm{CG}_2 \times \mathrm{RT}_1 \times \mathrm{DG}_0$	CG_2	RT_1	DG_0
	$\mathrm{CG}_2 \times \mathrm{CG}_2 \times \mathrm{CG}_1$	CG_2	CG_2	CG_1
	$\mathrm{CG}_2^+ \times \mathrm{CG}_2^+ \times \mathrm{DG}_1$	CG_2^+	CG_2^+	DG_1

Table 1: Two- ($\boldsymbol{u}\times p$) and three-field ($\boldsymbol{u}\times\boldsymbol{v}\times p$) formulations are presented their choices of function space. $\mathrm{CG_k}$, $\mathrm{EG_k}$, $\mathrm{DG_k}$, $\mathrm{RT_k}$, and $\mathrm{CG_k^+}$ refer to continuous Galerkin, enriched Galerkin, discontinuous Galerkin, Raviart-Thomas, and continuous Galerkin enriched by bubble function with polynomial degree k approximation function space.

The classical form of $\mathrm{CG}_2 \times \mathrm{CG}_1$ method is well-known to suffer from lack of the local mass conservation and producing unphysical (spurious) pressure oscillation (Haga et al., 2012; Choo and Lee, 2018; Kadeethum et al., 2019). This problem affects not only velocity calculation and coupling with the transport equation but also rock porosity and permeability alterations, which are determined by either the effective stress or the volumetric strain. This inaccuracy influences both the reservoir compaction and the conductivity alteration effects on the media's ability to deliver or withhold the desired fluid. Even though three-field formulation was developed to mitigate this problem, the unphysical pressure oscillation still occurs in $\mathrm{CG}_2 \times \mathrm{CG}_2 \times \mathrm{CG}_1$ space (Haga et al., 2012). In this study, we evaluate the performance of the six aforementioned methods by comparing: **1)** the local mass conservation property, **2)** the flux approximation, and **3)** the computational cost, i.e. degrees of freedom (DOF) and maximum time step, Δt.

2 Results and discussion

The example presented in this section is adapted from Kadeethum et al. (2019), and its geometry and boundary conditions are presented in Figure 1. The first investigation focuses on the local mass conservation, $\mathrm{r_{mass}}$, which is calculated as:

$$\mathrm{r}^n_{\mathrm{mass}} = \int_T \left[\rho\left(\phi c_f + \frac{\alpha - \phi}{K_s}\right)\frac{p^n - p^{n-1}}{\Delta t} + \rho\alpha\nabla\cdot\frac{\boldsymbol{u}^n - \boldsymbol{u}^{n-1}}{\Delta t}\right] dV + \sum_{e\in\varepsilon_h}\int_e \boldsymbol{v}^n\cdot\boldsymbol{n}|_{\mathrm{e}}\, dS \tag{7}$$

where $(.)^n$ and $(.)^{n-1}$ are current and previous time steps, respectively, and $\int_T XdV$ and $\int_e XdS$ refer to volume and surface integrals, respectively. Details of calculation can be found in Choo and Lee (2018) and Kadeethum et al. (2019). Figure 2 presents the maximum $\mathrm{r_{mass}}$, $\max(\mathrm{r_{mass}})$, at each time step, $\mathrm{CG_2 \times CG_1}$ and $\mathrm{CG_2 \times CG_2 \times CG_1}$ show a lack of local mass conservation property, and their $\max(\mathrm{r_{mass}})$ value is significantly high in the beginning (1×10^{-3} kg) and reduces as the flux becomes lower (Figure 2a). $\mathrm{CG_2 \times EG_1}$, $\mathrm{CG_2 \times DG_1}$, $\mathrm{CG_2 \times RT_1 \times DG_0}$, and $\mathrm{CG_2^+ \times CG_2^+ \times DG_1}$ methods, on the other hand, conserve local mass and, they have much less $\max(\mathrm{r_{mass}})$ value (Figure 2b). Moreover, the cases with smaller K values (more deformable) have higher $\max(\mathrm{r_{mass}})$ values than the cases that have larger K values (less deformable).

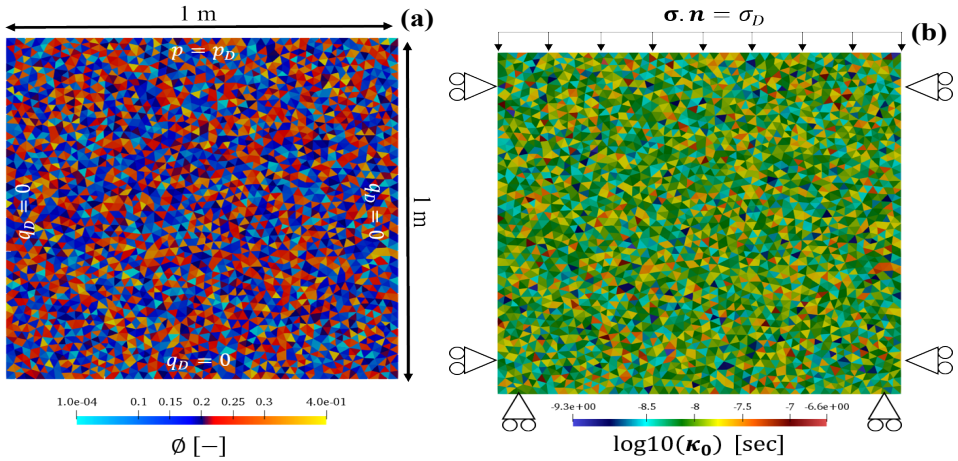

Figure 1: (**a**) ϕ field and mass boundary conditions and (**b**) $\log10(\boldsymbol{\kappa}_0)$ field and force boundary conditions (Kadeethum et al., 2019)

Subsequently, we investigate the error in the flux approximation, which is caused by the lack of local mass conservation. The quantity of interest is set to be recovery factor (RF) because it helps the comparison become clearer (Kadeethum et al., 2019). Figures 2c-e present the value of RF for case 1, $K = 8$ GPa, case 2, $K = 2$ GPa, and case 3, $K = 1$ GPa, respectively. There are three main observations drawn from these figures.

1. $\mathrm{CG_2 \times CG_1}$ and $\mathrm{CG_2 \times CG_2 \times CG_1}$ methods, which do not have a local mass conservation property and exhibit the unphysical oscillations at interfaces where large conductivity difference is observed (Haga et al., 2012; Kadeethum et al., 2019), provide higher RF approximation than other methods, which may lead to an overestimation of the flux approximation. Moreover, the differences between these methods and the methods that local mass is well preserved grow when the K value decreases.

2. Among the local mass conservative methods, $\mathrm{CG_2 \times EG_1}$, $\mathrm{CG_2 \times DG_1}$, and $\mathrm{CG_2 \times RT_1 \times DG_0}$ methods produce approximately the same RF result. $\mathrm{CG_2^+ \times CG_2^+ \times DG_1}$ method, however, provides the RF approximation a little higher than the rest. Nevertheless, the differences are small comparing to the differences between the local mass conserved methods and the methods that do not conserve mass locally.

3. When the reservoir has lower K value, i.e. more deformable, RF becomes higher because of compaction effect. Figures 2c-e illustrate that the final RF is increased from 3.5×10^{-3} to 2.0×10^{-2} when K is reduced from 8 GPa to 1 GPa. This observation holds true despite the fact that the $\boldsymbol{k_m}$ reduction is larger in softer media (Figure 2f). Therefore, the compaction effect may dominate over $\boldsymbol{k_m}$ reduction effect on reservoir productivity.

Degrees of freedom (DOF) among all methods are compared in Table 2. $\mathrm{CG_2 \times CG_1}$ has the least DOF, but it does not have the local mass conservation property. Among the methods

that possess the local mass conservation property, $CG_2 \times EG_1$ method has the least DOF. The three-field formulation generally has higher DOF than two-field formulation because of the velocity field. This circumstance will become more pronounced when the model is extended to 3-Dimension.

Function space	**Mixed space**	**Displacement**	**Velocity**	**Pressure**
$CG_2 \times CG_1$	19,582	17,370	-	2,212
$CG_2 \times EG_1$	23,844	17,370	-	6,474
$CG_2 \times DG_1$	30,156	17,370	-	12,786
$CG_2 \times RT_1 \times DG_0$	28,105	17,370	6,473	4,262
$CG_2 \times CG_2 \times CG_1$	36,952	17,370	17,370	2,212
$CG_2^+ \times CG_2^+ \times DG_1$	64,574	25,894	25,894	12,786

Table 2: Number of degrees of freedom (DOF) are compared among all discussed methods.

The selection of time step size, Δt, is also a critical factor in this analysis since the $\boldsymbol{k_m}$ alteration is fully coupled to the system, which leads to solving the system of nonlinear algebraic equations. The solution may not be converged, when Δt is not appropriately selected. Among the local mass conservative methods, the solutions of $CG_2 \times EG_1$ and $CG_2 \times DG_1$ methods are able to converge with the Δt of 1.0 sec. $CG_2 \times RT_1 \times DG_0$ and $CG_2^+ \times CG_2^+ \times DG_1$ methods, however, could not converge with the same Δt. Hence Δt is reduced to 0.1 sec for these methods. This limitation may lead to a significant more computational cost requirement of $CG_2 \times RT_1 \times DG_0$ and $CG_2^+ \times CG_2^+ \times DG_1$ methods. The adaptive time step technique may be able to mitigate this circumstance.

References

Balay, S., S. Abhyankar, M. Adams, J. Brown, P. Brune, K. Buschelman, L. Dalcin, A. Dener, V. Eijkhout, W. Gropp, D. Kaushik, M. Knepley, D. May, L. C. McInnes, R. T. Mills, T. Munson, K. Rupp, P. Sanan, B. Smith, S. Zampini, H. Zhang, and H. Zhang (2018). PETSc Users Manual. Technical Report ANL-95/11 - Revision 3.10, Argonne National Laboratory.

Biot, M. (1941). General theory of three-dimensional consolidation. *Journal of applied physics 12*(2), 155–164.

Choo, J. and S. Lee (2018). Enriched galerkin finite elements for coupled poromechanics with local mass conservation. *Computer Methods in Applied Mechanics and Engineering 341*, 311–332.

Du, J. and R. C. K. Wong (2007). Application of strain-induced permeability model in a coupled geomechanics-reservoir simulator. *Journal of Canadian Petroleum Technology 46*(12), 55–61.

Haga, J. B., H. Osnes, and H. P. Langtangen (2012). On the causes of pressure oscillations in lowâpermeable and lowâcompressible porous media. *International Journal for Numerical and Analytical Methods in Geomechanics 36*(12), 1507–1522.

Kadeethum, T., H. Nick, S. Lee, C. Richardson, S. Salimzadeh, and F. Ballarin (2019). A Novel Enriched Galerkin Method for Modelling Coupled Flow and Mechanical Deformation in Heterogeneous Porous Media. In *53rd US Rock Mechanics/Geomechanics Symposium*, New York, NY, USA. American Rock Mechanics Association.

Lee, S., Y.-J. Lee, and M. F. Wheeler (2016). A locally conservative enriched Galerkin approximation and efficient solver for elliptic and parabolic problems. *SIAM Journal on Scientific Computing 38*(3), A1404—-A1429.

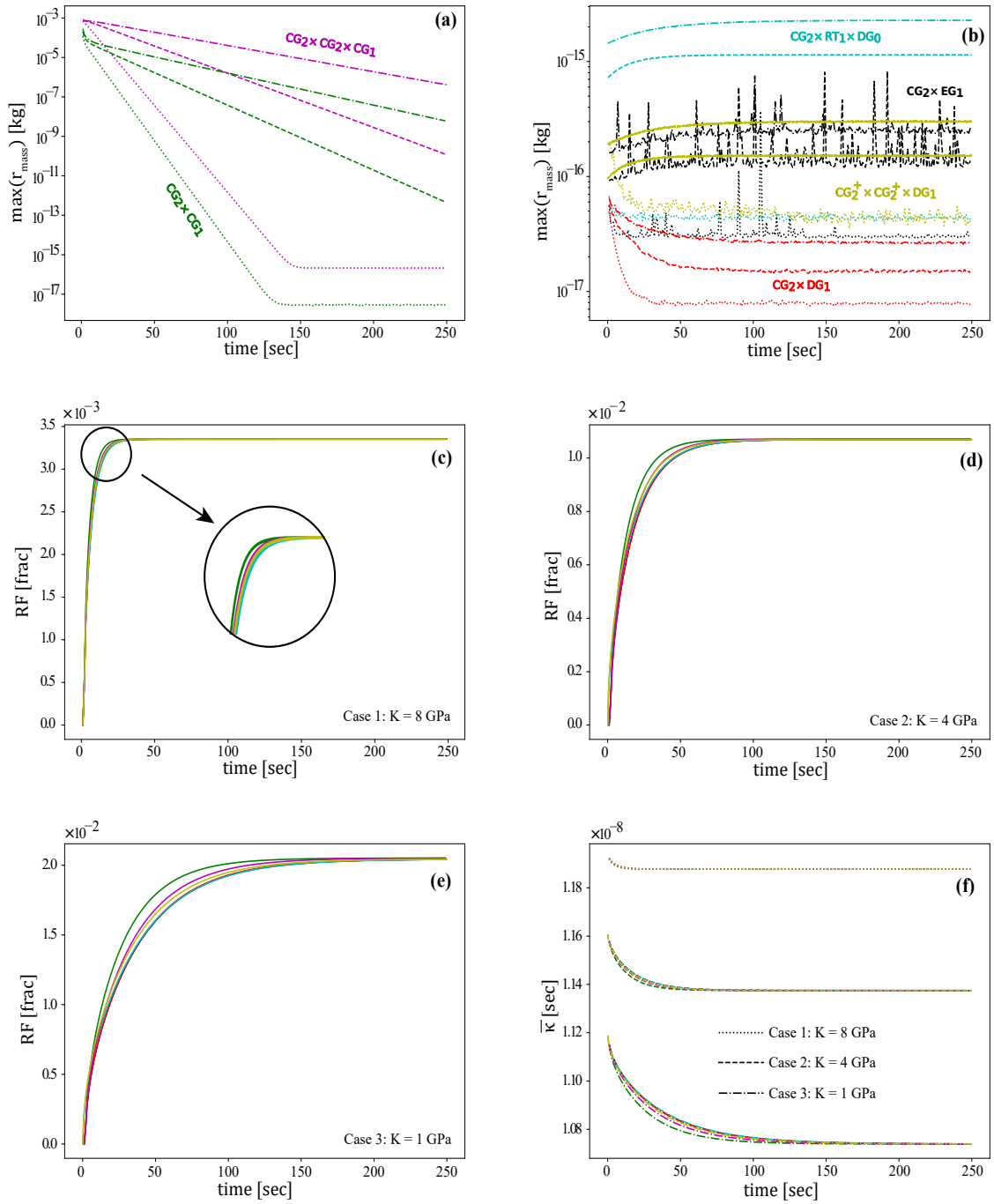

Figure 2: The comparison among $CG_2 \times CG_1$ (green line), $CG_2 \times EG_1$ (black line), $CG_2 \times DG_1$ (red line), $CG_2 \times CG_2 \times CG_1$ (magenta line), $CG_2 \times RT_1 \times DG_0$ (blue line), $CG_2^+ \times CG_2^+ \times DG_1$ (yellow line) methods for (**a**) and (**b**) $\max(r_{mass})$ among case 1 (.....), K = 8 GPa, case 2 (- - -), K = 2 GPa, and case 3 (-.-.-), K = 1 GPa and RF of all mentioned methods for (**c**) case 1, (**d**) case 2, (**e**) case 3, and (**f**) $\bar{\kappa}$ for all methods and cases.